A Convex Regularizer for Reducing Color Artifact in Color Image Recovery

Shunsuke Ono   Isao Yamada

Tokyo Institute of Technology, Japan

`ono/isao@sp.ce.titech.ac.jp`

Abstract

We propose a new convex regularizer, named the local color nuclear norm (LCNN), for color image recovery. The LCNN is designed to promote a property inherent in natural color images - in which their local color distributions often exhibit strong linearity - and is thus expected to reduce color artifact effectively. In addition, the very nature of LCNN allows us to incorporate it into various types of color image recovery formulations, with the associated convex optimization problems solvable using proximal splitting techniques. Applications of LCNN are demonstrated with illustrative numerical examples.

1. Introduction

Color image recovery problems, such as denoising, deblurring, demosaicking, inpainting, and super-resolution, are usually modeled as ill-posed or ill-conditioned inverse problems, and thus they require the use of a priori information for estimating an unknown original image satisfactorily. In general, the a priori information is exploited by a regularizer which is incorporated into the objective function to be minimized. Such a regularizer is desired to be convex in order to obtain a reasonable solution using computationally-efficient algorithms. Major convex regularizers for color image recovery are a family of *(isotropic) color/vectorial total variation* (CTVs) [3, 4, 14, 15, 16] which promote smoothness of color images while preserving edges, resulting in an effective noise reduction. On the other hand, however, they are not able to sufficiently reduce color artifact (see Figure 1 (c)).

Interestingly, one observes that in any local region of natural color images, its color (RGB) distribution is almost linear, as shown in Figure 1 (a). This property, which we shall refer to as the color line property, was first reported in [23], and has been utilized in image matting [18], dehazing [17], intrinsic imaging [29], and smoothing/denoising [30], to name a few. On the other hand, as shown in Figure 1 (c), the color line property is corrupted due to the existence of color artifact, which suggests that such color artifact is expected to be reduced by promoting the color line property.

With this in mind, we propose a novel convex regularizer inspired by the color line property, named *local color nuclear norm* (LCNN), for reducing artifact in color images. To incorporate the color line property into a convex regularizer, we first define a matrix, which we call *local color matrix*, consisting of the vectorized-and-horizontally-arranged RGB channel components of a local region of a color image (thus its column size is three), and then propose LCNN as the weighted sum of the singular values of each local color matrix of all regions. Since the column vectors (i.e., the RGB component vectors) of any local color matrix tend to be almost linearly dependent as long as the color line property is satisfied, the second and third singular values of the local color matrix are expected to be small (see Section 2 for a detailed account). This implies that, by choosing a small weight for the first singular value, suppressing LCNN promotes the color line property, yielding an efficient removal of color artifact. Moreover, the availability of the *proximity operator* of LCNN allows us to use LCNN as a building block for various color image recovery formulation, where the associated convex optimization problems can be solved using proximal splitting techniques. We present several useful applications of LCNN with examples which illustrate that color artifact is significantly reduced using LCNN.

2. Local Color Nuclear Norm

In what follows, $\mathbb{N}$ denotes the set of positive integers, $\mathbb{R}$, $\mathbb{R}_+$, and $\mathbb{R}_{++}$ the sets of all, nonnegative, and positive real numbers, respectively. Let $\mathcal{U} := \mathbb{R}^{n_v \times n_h} \times \mathbb{R}^{n_v \times n_h} \times \mathbb{R}^{n_v \times n_h}$ ($n_v, n_h \in \mathbb{N}$ correspond to image size) be a Euclidean (product) space equipped with the standard inner product $\langle \cdot, \cdot \rangle_{\mathcal{U}}$ and its induced norm $\| \cdot \|_{\mathcal{U}}$ (i.e., $(\mathcal{U}, \langle \cdot, \cdot \rangle_{\mathcal{U}}, \| \cdot \|_{\mathcal{U}})$ is a real Hilbert space). Consider a color image $\mathbf{U} := (\mathbf{U}_1, \mathbf{U}_2, \mathbf{U}_3) \in \mathcal{U}$ where $\mathbf{U}_l$ ($l = 1, 2, 3$) are its RGB channels, and let $\mathcal{I}_k^{\mathbf{U}}$ ($k = 1, \ldots, K$) be the index set of the pixels in the k-th non-overlapped local region (e.g., a block) of the color image $\mathbf{U}$, and $|\mathcal{I}_k^{\mathbf{U}}|$ the number of indices in $\mathcal{I}_k^{\mathbf{U}}$, i.e., the number of the pixels in the k-th region. We then define the local color matrix of the k-th region by

$$\mathbf{C}_{\mathcal{I}_k^{\mathbf{U}}} := \begin{bmatrix} \mathbf{c}_{1,k}^{\mathbf{U}} & \mathbf{c}_{2,k}^{\mathbf{U}} & \mathbf{c}_{3,k}^{\mathbf{U}} \end{bmatrix} \in \mathbb{R}^{|\mathcal{I}_k^{\mathbf{U}}| \times 3}, \qquad (1)$$

(a) Original (b) Noisy (salt-and-pepper) (c) Conventional (CTV-ℓ^1) (d) Proposed (CTV-LCNN-ℓ^1)
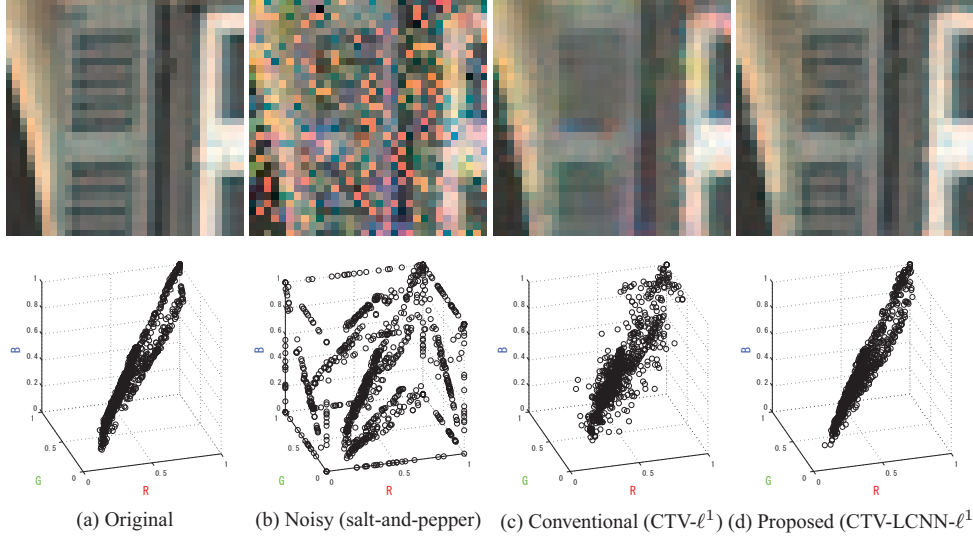
Figure 1: Local region and its color distribution: Observe that the local RGB channel components of the original image are linearly distributed (a), and the property (color line property) is lost by noise (b). The conventional approach cannot reduce color artifact sufficiently, so that the color line property is still corrupted (c). In contrast, the proposed method well recovers the color line property, resulting in an effective color artifact removal (d).
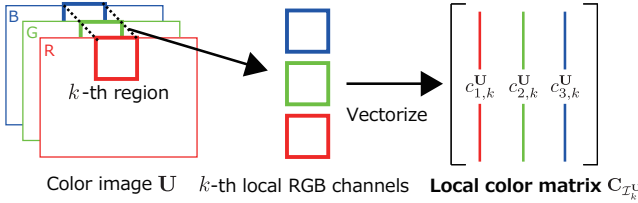

Figure 2: Flowchart of the construction of the local color matrix of the k-th region.

where $\mathbf{c}_{l,k}^{\mathbf{U}} \in \mathbb{R}^{|\mathcal{I}_k^{\mathbf{U}}|}$ ($l = 1, 2, 3$) are the vectorized k-th local RGB channels of $\mathbf{U}$, each of which consists of the lexicographically ordered channel components whose indices belong to $\mathcal{I}_k^{\mathbf{U}}$. To shed more light into the construction of local color matrices, we give its flowchart in Figure 2. The singular value decomposition of $\mathbf{C}_{\mathcal{I}_k^{\mathbf{U}}}$ is given by

$$\mathbf{C}_{\mathcal{I}_k^{\mathbf{U}}} = \mathbf{P}_{\mathcal{I}_k^{\mathbf{U}}} \mathbf{\Sigma}_{\mathcal{I}_k^{\mathbf{U}}} \mathbf{Q}_{\mathcal{I}_k^{\mathbf{U}}}^t,$$

where

$$\mathbf{\Sigma}_{\mathcal{I}_k^{\mathbf{U}}} := \text{diag}(\sigma_1(\mathbf{C}_{\mathcal{I}_k^{\mathbf{U}}}), \sigma_2(\mathbf{C}_{\mathcal{I}_k^{\mathbf{U}}}), \sigma_3(\mathbf{C}_{\mathcal{I}_k^{\mathbf{U}}})) \in \mathbb{R}_+^{|\mathcal{I}_k^{\mathbf{U}}| \times 3}$$

is a diagonal matrix which contains the singular values in descending order, and $\mathbf{P}_{\mathcal{I}_k^{\mathbf{U}}} \in \mathbb{R}^{|\mathcal{I}_k^{\mathbf{U}}| \times |\mathcal{I}_k^{\mathbf{U}}|}$ and $\mathbf{Q}_{\mathcal{I}_k^{\mathbf{U}}} \in \mathbb{R}^{3 \times 3}$ are some orthogonal matrices ($\cdot^t$ stands for the transposition). Using the local color matrix, our proposed regularizer named *local color nuclear norm* (LCNN) $\| \cdot \|_{\text{LC}*}$ is defined as follows:

$$\| \cdot \|_{\text{LC}*}^{\mathbf{w}} : \mathcal{U} \to [0, \infty) : \mathbf{U} \mapsto \sum_{k=1}^{K} \sum_{s=1}^{3} w_s \sigma_s(\mathbf{C}_{\mathcal{I}_k^{\mathbf{U}}}),$$

where $\mathbf{w} := [w_1 \ w_2 \ w_3]^t \in \mathbb{R}_{++}^3$. It is clear that if a local region has the color line property then the corresponding

local color vectors $\mathbf{c}_{l,k}^{\mathbf{U}}$ ($l = 1, 2, 3$) become almost linearly dependent, and vice versa. This means that the second and third singular values of any local color matrix $\mathbf{C}_{\mathcal{I}_k^{\mathbf{U}}}$ of natural color images are expected to be small, and this is violated by color artifact. Hence, by setting the weight w_1 to a small value and suppressing LCNN, we can promote the color line property, leading to the reduction of color artifact.

Proposition 2.1. $\| \cdot \|_{\text{LC}*}^{\mathbf{w}}$ *is a norm of* $\mathcal{U}$, *i.e.,* $\| \cdot \|_{\text{LC}*}^{\mathbf{w}}$ *satisfies the following properties: (i) For any* $\mathbf{U} \in \mathcal{U}$, $\|\mathbf{U}\|_{\text{LC}*}^{\mathbf{w}} \geq 0$ *and* $\|\mathbf{U}\|_{\text{LC}*}^{\mathbf{w}} = 0 \Leftrightarrow \mathbf{U} = \mathbf{O}$; *(ii) For any* $\mathbf{U}, \mathbf{U}' \in \mathcal{U}$, $\|\mathbf{U} + \mathbf{U}'\|_{\text{LC}*}^{\mathbf{w}} \leq \|\mathbf{U}\|_{\text{LC}*}^{\mathbf{w}} + \|\mathbf{U}'\|_{\text{LC}*}^{\mathbf{w}}$; *(iii) For any* $\alpha \in \mathbb{R}$ *and* $\mathbf{U} \in \mathcal{U}$, $\|\alpha\mathbf{U}\|_{\text{LC}*}^{\mathbf{w}} = |\alpha| \|\mathbf{U}\|_{\text{LC}*}^{\mathbf{w}}$.

Since $\| \cdot \|_{\text{LC}*}^{\mathbf{w}} \in \Gamma_0(\mathcal{U})$[1] by Proposition 2.1, we can define the proximity operator [21][2] of LCNN, which plays a central role in minimizing objective functions involving LCNN. By letting $\mathbf{\Sigma}_{\mathcal{I}_k^{\mathbf{U}}}^{\text{shr}} \in \mathbb{R}^{|\mathcal{I}_k^{\mathbf{U}}| \times 3}$ be a diagonal matrix with its diagonal elements being the singular values shrunk respectively by $w_i \gamma \in (0, \infty)$ ($i = 1, 2, 3$), i.e.,

$$\mathbf{\Sigma}_{\mathcal{I}_k^{\mathbf{U}}}^{\text{shr}} := \text{diag}(\max\{\sigma_1(\mathbf{C}_{\mathcal{I}_k^{\mathbf{U}}}) - w_1\gamma, 0\},$$
$$\ldots, \max\{\sigma_3(\mathbf{C}_{\mathcal{I}_k^{\mathbf{U}}}) - w_3\gamma, 0\}), \quad (2)$$

---

[1] Let $\mathcal{H}$ be a real Hilbert space equipped with the standard inner product $\langle \cdot, \cdot \rangle$ and its induced norm $\| \cdot \|$. A function $f : \mathcal{H} \to (-\infty, \infty]$ is called *proper lower semicontinuous convex* if $\text{dom}(f) := \{\mathbf{x} \in \mathcal{H} | f(\mathbf{x}) < \infty\} \neq \emptyset$, $\text{lev}_{\leq \alpha}(f) := \{\mathbf{x} \in \mathcal{H} | f(\mathbf{x}) \leq \alpha\}$ is closed for every $\alpha \in \mathbb{R}$, and $f(\lambda\mathbf{x} + (1 - \lambda)\mathbf{y}) \leq \lambda f(\mathbf{x}) + (1 - \lambda)f(\mathbf{y})$ for every $\mathbf{x}, \mathbf{y} \in \mathcal{H}$ and $\lambda \in (0, 1)$, respectively. The set of all proper lower semicontinuous convex functions on $\mathcal{H}$ is denoted by $\Gamma_0(\mathcal{H})$.

[2] For any $\gamma \in (0, \infty)$, the *proximity operator* of $f \in \Gamma_0(\mathcal{H})$ is given by $\text{prox}_{\gamma f}(\mathbf{x}) := \arg\min_{\mathbf{y} \in \mathcal{H}}\{f(\mathbf{y}) + \frac{1}{2\gamma}\|\mathbf{x} - \mathbf{y}\|^2\}$.

Figure 3: 15 test images (128×128).

the proximity operator of LCNN is then given by

$$\text{prox}_{\gamma\|\cdot\|^{\mathbf{w}}_{\text{LC}*}} : \mathcal{U} \to \mathcal{U} : \mathbf{U} \mapsto \mathbf{U}^{\text{shr}},$$

where $\mathbf{U}^{\text{shr}}$ is the color image such that its local color matrix $\mathbf{C}_{\mathcal{I}^{\mathbf{U}^{\text{shr}}}_k}$ is equal to $\mathbf{P}_{\mathcal{I}^{\mathbf{U}}_k} \mathbf{\Sigma}^{\text{shr}}_{\mathcal{I}^{\mathbf{U}}_k} \mathbf{Q}^t_{\mathcal{I}^{\mathbf{U}}_k}$ for $k = 1, \ldots, K$. In other words, the computation of $\text{prox}_{\gamma\|\cdot\|^{\mathbf{w}}_{\text{LC}*}}$ is equivalent to constructing the local color matrices from the input color image, performing singular value shrinkage to each of them as in (2), and reconstructing the output color image. We remark that the availability of the proximity operator of LCNN allows us to utilize computationally-efficient proximal splitting algorithms for solving convex optimization problems involving LCNN. The interested reader is referred to, e.g., [32, 8, 2] for recent developments in convex analysis and optimization that are related to this work.

3. Applications

Thanks to its simple but special property, LCNN has a potential to serve as a fundamental and effective tool in color image recovery and further applications. In the following, we provide useful applications of LCNN to several image recovery problems. Corresponding experiments were performed using MATLAB (R2013a), on a Windows 7 (64bit) desktop computer with an Intel Core i7 2.8 GHz processor and 8.0 GB of RAM. All test images[3] (Figure 3) are normalized with intensity range of $[0, 1]$. We pick up each local region of LCNN as simply a $b \times b$ square block, where $b \in \mathbb{N}$ is set to a suitable value for each application. The weight of LCNN is fixed at $\mathbf{w} = [0.01 \; 1 \; 1]$.

3.1. Denoising

Denoising is a basic task in many image processing and computer vision applications. Let us consider to estimate an unknown original color image $\overline{\mathbf{U}} \in \mathcal{U}$ from a given noisy image $\mathbf{V} = \mathcal{D}(\overline{\mathbf{U}})$, where we focus on the two contamination cases: $\mathcal{D}$ either denotes an additive white Gaussian noise with the standard deviation $\sigma \in \mathbb{R}_{++}$ or an impulsive noise with the probability $p \in (0, 1)$.

3.1.1 Gaussian noise case

Much research has been devoted to image denoising under Gaussian noise contamination, and state-of-the-art performance can be achieved using patch-based nonlocal methods, e.g., [11, 19]. It is also true, however, that there is room

for improvement in terms of the reduction of color artifact. Our method is thus formulated as follows: find

$$\mathbf{U}^\star = \arg\min_{\mathbf{U}\in\mathcal{U}}\{\lambda\|\mathbf{U}\|^{\mathbf{w}}_{\text{LC}*} + \tfrac{1}{2}\|\mathbf{U} - \mathbf{U}_{\text{pre}}\|^2_{\mathcal{U}}\}, \quad (3)$$

where $\mathbf{U}_{\text{pre}}$ is a preprocessed image generated by some denoising method. This hybrid approach realizes an effective denoising+color artifact reduction under Gaussian noise contamination. Clearly, problem 3 is equivalent to calculating $\text{prox}_{\lambda\|\mathbf{U}\|^{\mathbf{w}}_{\text{LC}*}}(\mathbf{U}_{\text{pre}})$, so that it can be readily solved by applying the singular value shrinkage only once.

The experimental results for $\sigma = 0.15$ are shown in Table 1 and Figure 4, where we observe that the proposed method ($\lambda = 0.35$, $b = 32$, $\mathbf{U}_{\text{pre}}$ is obtained by the CBM3D denoising [11]) improves the recovery performance of CBM3D both in terms of objective measure (PSNR [dB] and CIEDE2000 [28][4]) and human eye perception. The average CPU times of CBM3D and the additional LCNN color artifact reduction step are about 0.16 and 0.13 seconds, respectively.

3.1.2 Impulsive noise case

Things change in the inpulsive noise contamination case, where standard denoising methods assuming Gaussian distribution usually fail to give a reasonable estimate. In such a situation, convex optimization-based strategies using the (C)TV-ℓ^1 model are known as a very powerful approach, as investigated in [12, 6, 16]. On the other hand, as in the Gaussian case, color degradation caused by color artifact is not completely inevitable even using the CTV-ℓ^1 model. This leads to the proposed formulation: find

$$\mathbf{U}^\star \in \arg\min_{\mathbf{U}\in C_{[0,1]}\cap C^1_{\mathbf{V},\varepsilon}}\{\lambda\|\mathbf{U}\|_{\text{CTV}} + \|\mathbf{U}\|^{\mathbf{w}}_{\text{LC}*}\}, \quad (4)$$

where $C_{[0,1]} := \{\mathbf{U} \in \mathcal{U}| \; U_{l_{i,j}} \in [0,1] \; \forall(l,i,j)\}$ ($\cdot_{l_{i,j}}$ the (i,j)-th entry of the l-th channel of $\cdot$) denotes a pixel intensity constraint, $C^1_{\mathbf{V},\varepsilon} := \{\mathbf{U} \in \mathcal{U}| \; \|\mathbf{U} - \mathbf{V}\|_1 := \sum_{l,i,j}|U_{l_{i,j}} - V_{l_{i,j}}| \leq \varepsilon\}$ the $\mathbf{V}$-centered ℓ^1 ball for the data-fidelity (under impulsive noise contamination), and $\|\cdot\|_{\text{CTV}}$ the CTV. In our method, the CTV proposed in [4, 14] is employed because it achieves a better performance compared to other CTVs [3, 15, 16] in the applications presented in this paper. The reason why we adopt the constrained formulation instead of the standard unconstrained one (i.e., adding the ℓ^1 fidelity term to the objective function) is that the fidelity level ε can be adjusted in a relatively easy manner based on some statistical information (e.g., p).

---

[3] Some of the test images are available at http://r0k.us/graphics/kodak/ and www.mayang.com/textures.

[4] CIEDE2000 is known as a better color quality assessment compared with PSNR (a smaller value of CIEDE2000 indicates a higher quality).

Table 1: Comparison of PSNR and CIEDE2000 in Gaussian denoising (corresponding to the order of Figure 3)

| CBM3D | PSNR [dB] | 27.39 | 25.60 | 26.36 | 28.20 | 31.94 | 27.19 | 27.89 | 30.20 | 23.58 | 26.68 | **28.29** | 26.90 | 25.25 | 28.37 | **24.59** |
	CIEDE2000	4.90	6.46	5.13	4.20	3.52	4.87	4.51	3.82	7.46	5.36	4.23	4.83	6.82	2.20	7.24
Proposed	PSNR [dB]	**27.48**	**25.81**	**26.47**	**28.37**	**32.46**	**27.35**	**28.12**	**30.35**	**23.62**	**26.74**	28.28	**27.08**	**25.30**	**28.98**	24.55
	CIEDE2000	**4.38**	**5.44**	**4.88**	**3.63**	**2.04**	**4.12**	**3.80**	**3.19**	7.24	**4.67**	**4.12**	**4.05**	**6.28**	**1.60**	**6.98**
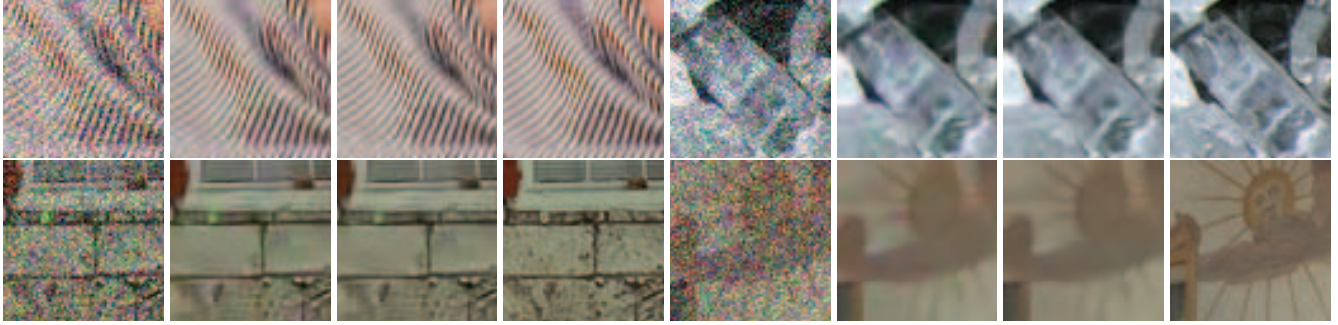
Figure 4: Closeup of some Gaussian ($\sigma = 0.15$) denoising results : From left, Noisy; CBM3D; CBM3D+LCNN (proposed); Original.

It appears much difficult to solve problem 4 owing to its highly non-smooth nature. Fortunately, however, recent significant advances in convex optimization bring out an efficient algorithmic solution to such a problem with the help of proximal splitting techniques. In particular, primal-dual splitting type algorithms, e.g., [5, 9, 10], are known as among the most flexible solvers in the sense that they are free from operator inversion in their iteration. We utilize in this paper the primal-dual splitting method [10], which can solve the following nonsmooth convex optimization problem[5]: find

$$\mathbf{x}^\star \in \arg\min_{\mathbf{x} \in \mathcal{H}} \{g(\mathbf{x}) + h(L\mathbf{x})\}, \qquad (5)$$

where $g \in \Gamma_0(\mathcal{H})$, $h \in \Gamma_0(\mathcal{G})$, and $L : \mathcal{H} \to \mathcal{G}$ is a bounded linear operator ($\mathcal{H}$ and $\mathcal{G}$ denote real Hilbert spaces). A simple version of the primal-dual splitting method iteratively computes the following steps:

$$\left| \begin{array}{l} \mathbf{x}_{n+1} = \mathrm{prox}_{\gamma_1 g}[\mathbf{x}_n - \gamma_1 L^* \mathbf{y}_n] \\ \mathbf{y}_{n+1} = \mathrm{prox}_{\gamma_1 h^*}[\mathbf{y}_n + \gamma_2 L(2\mathbf{x}_{n+1} - \mathbf{x}_n)], \end{array} \right. \qquad (6)$$

where h^* is the *Fenchel-Rockafellar conjugate function*[6] of h, L^* the adjoint of L, and $\gamma_1, \gamma_2 \in \mathbb{R}_{++}$. It is known that, by assuming $\gamma_1^{-1} - \gamma_2 \|L\|_{op}^2 > 0$ ($\|\cdot\|_{op}$ stands for the operator norm), the pair of sequences $(\mathbf{x}_n, \mathbf{y}_n)$ generated by algorithm 6 (weakly) converges to the solution of problem 5 and its dual.

Now let $\mathcal{H} := \mathcal{U}, \mathcal{G} := \mathcal{U} \times \mathcal{U} \times \mathcal{U} \times \mathcal{U}, g(\mathbf{U}) := \|\mathbf{U}\|_{\mathrm{LC}*}$, $L(\mathbf{U}) := (\mathbf{D}_v(\mathbf{U}), \mathbf{D}_h(\mathbf{U}), \mathbf{U}, \mathbf{U})$, and $h(\Theta_1, \ldots, \Theta_4) := \|(\Theta_1, \Theta_2)\|_{1,2} + \iota_{C_{[0,1]}}(\Theta_3) + \iota_{C_{\mathbf{V},\varepsilon}^1}(\Theta_4)$, where $\mathbf{D}_v, \mathbf{D}_h$ are discrete vertical and horizontal difference operators,

$\|(\cdot, \cdot)\|_{1,2} := \sum_{i=1}^{n_v} \sum_{j=1}^{n_h} \sqrt{\sum_{l=1}^3 X_{l_{i,j}}^2 + Y_{l_{i,j}}^2}$, and ι. the indicator function[7] of the nonempty convex set $\cdot$. Note that the CTV can be expressed as $\|\mathbf{U}\|_{\mathrm{CTV}} = \|(\mathbf{D}_v(\mathbf{U}), \mathbf{D}_h(\mathbf{U}))\|_{1,2}$. Problem 5 then becomes equivalent to Problem 4, resulting in a solver for problem 4 via the primal-dual splitting method as shown in Algorithm 3.1. In the algorithm, we need to compute the proximity operator of $\|(\cdot, \cdot)\|_{1,2}$, which is given by

$$\mathrm{prox}_{\gamma \|(\cdot, \cdot)\|_{1,2}}(\mathbf{X}, \mathbf{Y}) := \{1 - \tfrac{\gamma}{d_{i,j}}, 0\}. * (\mathbf{X}, \mathbf{Y}),$$

where $d_{i,j} := \sqrt{\sum_{l=1}^3 X_{l_{i,j}}^2 + Y_{l_{i,j}}^2}$, and $.*$ stands for entry-wise multiplication. The metric projections onto $C_{[0,1]}$ and $C_{\mathbf{V},\varepsilon}$ are also required, and they are respectively obtained by pushing pixel values out of $[0, 1]$ into 0 or 1 (the nearest one is chosen) and a fast ℓ^1 ball projection technique [13]. Algorithm 3.1 is computationally efficient because it does not require operator inversion and inner loop.

The experimental results are given in Table 2 and Figure 5, where the test images are contaminated by a salt-and-pepper noise with probability $p = 0.3$. To verify the effectiveness of LCNN in a fair way, we compare the performance of the proposed method with that of the CTV-ℓ^1 method which is equivalent to solving problem 4 without the LCNN term. Algorithm 3.1 is utilized in both methods ($\gamma_1 = \gamma_2 = 0.35$ and the stopping criterion $\|\mathbf{U}_{n+1} - \mathbf{U}_n\|_\mathcal{U} < 0.01$). The fidelity level ε of both methods are set to $0.5 n_v n_h \sigma$. In contrast to the CTV-ℓ^1 method, the proposed method ($\lambda = 0.13$, $b = 8$) restores a color-artifact-free denoised image as shown in Figure 5. The average CPU time and iteration number of the CTV-ℓ^1 method are about 45 seconds and 331, and those of the proposed method are about 26 seconds and 183, implying that

---

[5] To be more precise, the primal-dual splitting method admits an additional differentiable function of which Lipschitzian gradient is computable.

[6] The *Fenchel-Rockafellar conjugate function* of $f \in \Gamma_0(\mathcal{H})$ is defined by $f^*(\xi) := \sup_{\mathbf{x} \in \mathcal{H}} \{\langle \mathbf{x}, \xi \rangle - f(\mathbf{x})\}$. The proximity operator of f^* can be expressed as $\mathrm{prox}_{\gamma f^*}(\mathbf{x}) = \mathbf{x} - \gamma \mathrm{prox}_{\gamma^{-1} f}(\gamma^{-1} \mathbf{x})$.

[7] For a given nonempty convex set $C \subset \mathcal{H}$, the indicator function $\iota_C \in \Gamma_0(\mathcal{H})$ is defined by $\iota_C(\mathbf{x}) := 0$ if $\mathbf{x} \in C$, ∞ otherwise. The proximity operator of ι_C coincides with the metric projection onto C.

Table 2: Comparison of PSNR and CIEDE2000 in salt-and-pepper denoising (corresponding to the order of Figure 3)

TV-ℓ^1	PSNR [dB]	22.21	25.51	26.20	29.19	37.41	25.62	24.23	32.36	22.95	26.02	25.12	26.86	23.64	23.54	24.05
	CIEDE2000	7.05	5.94	3.89	2.74	1.75	5.11	4.92	2.17	7.59	3.50	3.07	4.18	6.75	2.11	6.36
Proposed	PSNR [dB]	**24.99**	**28.16**	**27.03**	**30.81**	**41.31**	**28.17**	**27.54**	**34.42**	**24.30**	**26.36**	**27.22**	**29.71**	**25.71**	**26.69**	**25.35**
	CIEDE2000	**4.01**	**3.56**	**3.73**	**2.07**	**0.38**	**2.71**	**2.80**	**1.58**	**5.80**	**3.09**	**2.58**	**2.72**	**4.99**	**0.91**	**5.24**

Figure 5: Closeup of some salt-and-pepper ($p = 0.3$) denoising results: From left, Noisy; CTV-ℓ^1; CTV-LCNN-ℓ^1 (proposed); Original.

Algorithm 3.1 Solver for problem 4

1: Set $n = 0$. Choose $\mathbf{U}^{(0)} \in \mathcal{U}$, and $\varepsilon, \gamma_1, \gamma_2 \in \mathbb{R}_+$.
2: $(\boldsymbol{\Theta}_1^{(0)}, \ldots, \boldsymbol{\Theta}_4^{(0)}) = (\mathbf{D}_v(\mathbf{U}^{(0)}), \mathbf{D}_h(\mathbf{U}^{(0)}), \mathbf{U}^{(0)}, \mathbf{U}^{(0)})$
3: **while** a stop criterion is not satisfied **do**
4: $\quad \widehat{\mathbf{U}} = \mathbf{U}^{(n)} - \gamma_1(\mathbf{D}_v^t(\boldsymbol{\Theta}_1^{(n)}) + \mathbf{D}_h^t(\boldsymbol{\Theta}_2^{(n)}) + \boldsymbol{\Theta}_3^{(n)} + \boldsymbol{\Theta}_4^{(n)})$
5: $\quad \mathbf{U}^{(n+1)} = \text{prox}_{\|\cdot\|_{\text{LC}*}^{\mathbf{w}}}(\widehat{\mathbf{U}})$
6: $\quad \boldsymbol{\Lambda}_1^{(n)} = \boldsymbol{\Theta}_1^{(n)} + \gamma_2\mathbf{D}_v(2\widehat{\mathbf{U}}^{(n)} - \mathbf{U}^{(n)})$
7: $\quad \boldsymbol{\Lambda}_2^{(n)} = \boldsymbol{\Theta}_2^{(n)} + \gamma_2\mathbf{D}_h(2\widehat{\mathbf{U}}^{(n)} - \mathbf{U}^{(n)})$
8: $\quad \boldsymbol{\Lambda}_3^{(n)} = \boldsymbol{\Theta}_3^{(n)} + \gamma_2(2\widehat{\mathbf{U}}^{(n)} - \mathbf{U}^{(n)})$
9: $\quad \boldsymbol{\Lambda}_4^{(n)} = \boldsymbol{\Theta}_4^{(n)} + \gamma_2(2\widehat{\mathbf{U}}^{(n)} - \mathbf{U}^{(n)})$
10: $\quad (\widehat{\boldsymbol{\Lambda}}_1^{(n)}, \widehat{\boldsymbol{\Lambda}}_2^{(n)}) = \text{prox}_{\lambda\gamma_2^{-1}\|(\cdot,\cdot)\|_{1,2}}(\gamma_2^{-1}\boldsymbol{\Lambda}_1^{(n)}, \gamma_2^{-1}\boldsymbol{\Lambda}_2^{(n)})$
11: $\quad \widehat{\boldsymbol{\Lambda}}_3^{(n)} = P_{C_{[0,1]}}(\gamma_2^{-1}\boldsymbol{\Lambda}_3^{(n)})$
12: $\quad \widehat{\boldsymbol{\Lambda}}_4^{(n)} = P_{C_{\mathbf{V},\varepsilon}^1}(\gamma_2^{-1}\boldsymbol{\Lambda}_4^{(n)})$
13: $\quad$ **for** $m = 1$ to 4 **do**
14: $\quad\quad \boldsymbol{\Theta}_m^{(n+1)} = \boldsymbol{\Lambda}_m^{(n)} - \gamma_2\widehat{\boldsymbol{\Lambda}}_m^{(n)}$
15: $\quad$ **end for**
16: $\quad n = n + 1$
17: **end while**
18: Output $\mathbf{U}^{(n)}$

the use of LCNN leads to a faster convergence.

3.2. Simultaneous Deblurring and Inpainting

We proceed to consider a more involved case: estimating an original image $\overline{\mathbf{U}}$ from a noisy blurred image with missing pixels that can be modeled as $\mathbf{V} = \mathcal{D}(\mathbf{MB}(\overline{\mathbf{U}}))$, where $\mathbf{B} : \mathcal{U} \to \mathcal{U}$ is a blur operator, and $\mathbf{M} : \mathcal{U} \to \mathcal{U}$ a binary masking operator representing missing pixels. Here we simply consider additive white Gaussian noise contamination as $\mathcal{D}$. This general model covers various degradation scenarios, and, indeed, such a simultaneous restoration using TV (grayscale) has been studied, for example, in [7, 22]. We thus propose a simultaneous color image deblurring and

inpainting method: find

$$\mathbf{U}^\star \in \arg \min_{\mathbf{U} \in C_{[0,1]}, \, \mathbf{MB}(\mathbf{U}) \in C_{\mathbf{V},\varepsilon}^2} \{\lambda\|\mathbf{U}\|_{\text{CTV}} + \|\mathbf{U}\|_{\text{LC}*}^{\mathbf{w}}\}, \quad (7)$$

where $C_{\mathbf{V},\varepsilon}^2 := \{\mathbf{X} \in \mathcal{U}| \; \|\mathbf{X} - \mathbf{V}\|_{\mathcal{U}} \leq \varepsilon\}$ is the $\mathbf{V}$-centered Euclidean ball for the data-fidelity (under Gaussian noise contamination) onto which projection is given by $P_{C_{\mathbf{V},\varepsilon}^2}(\mathbf{X}) := \mathbf{X}$ if $\|\mathbf{X} - \mathbf{V}\|_{\mathcal{U}} \leq \varepsilon$, $\mathbf{V} + \frac{\varepsilon}{\|\mathbf{X} - \mathbf{V}\|_{\mathcal{U}}}(\mathbf{X} - \mathbf{V})$ otherwise. Problem 7 can also be solved via the primal-dual splitting method. The resulting algorithm is obtained by replacing steps 2, 4, 9, and 12 of Algorithm 3.1 respectively with

$$(\boldsymbol{\Theta}_1^{(0)}, \ldots, \boldsymbol{\Theta}_4^{(0)}) = (\mathbf{D}_v(\mathbf{U}^{(0)}), \mathbf{D}_h(\mathbf{U}^{(0)}), \mathbf{U}^{(0)}, \mathbf{MB}(\mathbf{U}^{(0)})),$$

$$\widehat{\mathbf{U}} = \mathbf{U}^{(n)} - \gamma_1(\mathbf{D}_v^t(\boldsymbol{\Theta}_1^{(n)}) + \mathbf{D}_h^t(\boldsymbol{\Theta}_2^{(n)}) + \boldsymbol{\Theta}_3^{(n)} + \mathbf{B}^*\mathbf{M}^*(\boldsymbol{\Theta}_4^{(n)})),$$

$$\boldsymbol{\Lambda}_4^{(n)} = \boldsymbol{\Theta}_4^{(n)} + \gamma_2\mathbf{MB}(2\widehat{\mathbf{U}}^{(n)} - \mathbf{U}^{(n)}),$$

$$\widehat{\boldsymbol{\Lambda}}_4^{(n)} = P_{C_{\mathbf{V},\varepsilon}^2}(\gamma_2^{-1}\boldsymbol{\Lambda}_4^{(n)}).$$

We show the experimental results in Table 3 and Figure 6. The degraded images were generated in such a way that the test images are blurred by a 3×3 Gaussian kernel, randomly missing about 40% pixels, and contaminated by an additive white Gaussian noise ($\sigma = 0.05$). The proposed method is compared with the CTV-ℓ^2 method which solves problem 7 without the LCNN term. Algorithm 3.1 with the above-mentioned replacement is used in both methods, where $\gamma_1 = \gamma_2 = 0.35$ and the stopping criterion is $\|\mathbf{U}_{n+1} - \mathbf{U}_n\|_{\mathcal{U}} < 0.001$. The fidelity level ε of both methods are set to $0.95\sqrt{0.4 n_v n_h}\sigma$. We observe in Figure 6 that the restored images by the proposed method ($\lambda = 0.07$, $b = 8$) have less color artifact compared with those of the CTV-ℓ^2 method. The average CPU time and iteration number of the CTV-ℓ^2 method are about 15 seconds and 1730, and those of the proposed method are about 12 seconds and 318. Compared with the salt-and-pepper denoising case, the computational cost of both methods are low because the

Table 3: Comparison of PSNR and CIEDE2000 in deblurring+inpainting (corresponding to the order of Figure 3)

TV-ℓ^2	PSNR [dB]	21.31	24.86	25.76	28.52	32.56	24.77	25.02	30.72	22.37	26.84	25.19	26.87	23.38	23.86	23.81
	CIEDE2000	6.97	6.43	4.53	3.69	3.38	5.36	4.86	3.33	7.82	4.24	**3.84**	4.39	6.91	2.88	6.85
Proposed	PSNR [dB]	**22.03**	**25.67**	**26.28**	**28.95**	**33.76**	**25.51**	**25.87**	**31.44**	**22.70**	**27.09**	**25.89**	**27.49**	**23.94**	**24.98**	**24.27**
	CIEDE2000	**5.95**	**5.14**	**4.46**	**3.26**	**2.05**	**4.48**	**4.09**	**2.83**	**7.44**	**3.98**	3.88	**3.81**	**6.25**	**2.22**	**6.65**
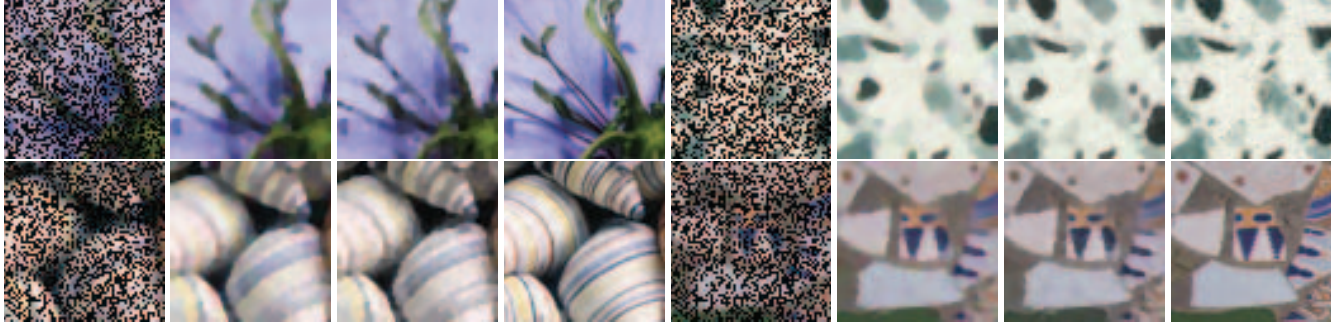
Figure 6: Closeup of some deblurring+inpainting ($\sigma = 0.05$) results: From left, Degraded; CTV-ℓ^2; CTV-LCNN-ℓ^2 (proposed); Original.

computation of $P_{C_{\mathbf{V},\varepsilon}^2}$ is much easier than that of $P_{C_{\mathbf{V},\varepsilon}^1}$, and, as in the case, the proposed method results in a faster convergence.

4. Discussion

4.1. Parameter Setting

There are two parameters regarding LCNN, i.e, the local region size b (the square block case) and λ that determines the relative importance between LCNN and the other functions to be minimized. On the setting of b, we can say that, basically, it should be a small value since the color line property is well satisfied in a small region. Moreover, a small b is better in terms of the computational cost of the singular value decomposition required in the computation of $\mathrm{prox}_{\gamma \| \cdot \|_{\mathrm{LC}*}^{\mathbf{w}}}$. However, in the case that color artifact spreads as in the preprocessed images in Figure 4, the region size b has to be chosen as a relatively large value to remove such color artifact. On the other hand, a suitable value of λ varies according to the application as has been seen in the previous section, and it is actually different depending on each image. However, even if the most suitable value is not chosen for individual images, the advantage of using LCNN is confirmed, as exhibited in the comparison of PSNR and CIEDE2000 of all the test images (Tables 4-6), where we adopted a single value for λ in each application.

4.2. Limitation

Evidently, LCNN cannot reduce noise only in the luminance component, so that it should be used together with another regularizer such as CTVs. It is also clear that, if an image to be estimated does not originally enjoy the color line property, then LCNN is useless and rather inconsistent.

5. Concluding Remarks

We have proposed a novel convex regularizer, named the local color nuclear norm (LCNN), for reducing color artifact in color image recovery. The LCNN is designed to promote what we call the color line property, which refers to the strong linearity often exhibited by the local color distribution of natural color images. Since the color line property is violated by color degradation, the LCNN serves to reduce the presence of color artifact. With the proximity operator of LCNN being computable, there is a variety of its possible applications via proximal splitting techniques which are not limited to the ones provided in this paper but also include, for example, those of using Moreau envelope in image recovery [26]. Experimental results illustrated the effectiveness, and, at the same time, suggest further potential of LCNN, both in terms of collaboration with other regularizers, such as the ℓ^1 norm of frame coefficients (e.g., wavelet), the convexified vectorial Mumford-Shah functional [31], the anisotropic vectorial L_∞ total variation [20], and the block nuclear norm [25], and applications, such as super resolution, demosaicking, and compressed sensing. It is also interesting to incorporate LCNN into image decomposition models (e.g., [1, 14, 24, 27, 22][8]), which may help to restore well-textured images. Future work includes an automatic parameter selection and an efficient parallel implementation based on the block-wise nature of LCNN.

Acknowledgements

---

[8] Schaeffer and Osher [27] proposed to use the nuclear norm of a matrix consisting of vectorized patches of (grayscale) images for characterizing texture. The construction procedure of the matrix appears similar to ours but it is actually completely different.

References

[1] J. F. Aujol and S. H. Kang. Color image decomposition and restoration. *J. Vis. Commun. and Image Repres.*, 17(4):916–928, 2006. 6

[2] H. H. Bauschke and P. L. Combettes. *Convex analysis and monotone operator theory in Hilbert spaces*. Springer, 2011. 3

[3] P. Blomgren and T. F. Chan. Color TV: Total variation methods for restoration of vector valued images. *IEEE Trans. Image Process.*, 7(3):304–309, 1998. 1, 3

[4] X. Bresson and T. F. Chan. Fast dual minimization of the vectorial total variation norm and applications to color image processing. *Inverse Probl. Imag.*, 2(4):455–484, 2008. 1, 3

[5] A. Chambolle and T. Pock. A first-order primal-dual algorithm for convex problems with applications to imaging. *J. Math. Imaging and Vision*, 40(1):120–145, 2010. 4

[6] R. H. Chan, Y. Dong, and M. Hintermüller. An efficient two-phase L^1-TV method for restoring blurred images with impulse noise. *IEEE Trans. Image Process.*, 19(7):1731–1739, 2010. 3

[7] T. F. Chan, A. M. Yip, and F. E. Park. Simultaneous total variation image inpainting and blind deconvolution. *Int. J. Imag. Syst. Tech.*, (1):92–102, 2005. 5

[8] P. L. Combettes and J.-C. Pesquet. Proximal splitting methods in signal processing. In H. H. Bauschke, R. S. Burachik, P. L. Combettes, V. Elser, D. R. Luke, and H. Wolkowicz, editors, *Fixed-Point Algorithms for Inverse Problems in Science and Engineering*. Springer-Verlag, 2011. 3

[9] P. L. Combettes and J.-C. Pesquet. Primal-dual splitting algorithm for solving inclusions with mixtures of composite, lipschitzian, and parallel-sum type monotone operators. *Set-Valued and Variational Analysis*, 20(2):307–330, 2012. 4

[10] L. Condat. A primal-dual splitting method for convex optimization involving Lipschitzian, proximable and linear composite terms. *J. Optimization Theory and Applications*, 2012. DOI 10.1007/s10957-012-0245-9. 4

[11] K. Dabov, A. Foi, V. Katkovnik, and K. Egiazarian. Color image denoising via sparse 3D collaborative filtering with grouping constraint in luminance-chrominance space. In *Proc. ICIP*, pages 313–316, 2007. 3

[12] Y. Dong, M. Hintermüller, and M. Neri. An efficient primal-dual method for L^1TV image restoration. *SIAM J. Imag. Sci.*, 2(4):1168–1189, 2009. 3

[13] J. Duchi, S. S-Shwartz, Y. Singer, and T. Chandra. Efficient projections onto the ℓ_1-ball for learning in high dimensions. In *Proc. of ICML*, pages 272–279, 2008. 4

[14] V. Duval, J. F. Aujol, and L. Vese. Mathematical modeling of textures : application to color image decomposition with a projected gradient algorithm. *J. Math. Imag. Vis.*, 37(3):232–248, 2010. 1, 3, 6

[15] B. Goldluecke and D. Cremers. An approach to vectorial total variation based on geometric measure theory. In *Proc. CVPR*, pages 327–333, 2010. 1, 3

[16] B. Goldluecke, E. Strekalovskiy, and D. Cremers. The natural vectorial total variation which arises from geometric measure theory. *SIAM J. Imag. Sci.*, 5(2):537–563, 2012. 1, 3

[17] K. He, J. Sun, and X. Tang. Single image haze removal using dark channel prior. *IEEE Trans. Pattern Anal. Mach. Intell.*, 33(12):2341–2353, 2011. 1

[18] A. Levin, D. Lischinski, and Y. Weiss. A closed-form solution to natural image matting. *IEEE Trans. Pattern Anal. Mach. Intell.*, 30(2):228–242, 2008. 1

[19] J. Mairal, F. Bach, J. Ponce, G. Sapiro, and A. Zisserman. Non-local sparse models for image restoration. In *Proc. IEEE ICCV*, pages 2272–2279, 2009. 3

[20] T. Miyata. Total variation defined by weighted l infinity norm for utilizing inter channel dependency. In *Proc. IEEE ICIP*, pages 3057–3060, 2012. 6

[21] J. J. Moreau. Proximité et dualité dans un espace hilbertien. *Bull. Soc. Math. France*, 93(2):273–299, 1965. 2

[22] M. K. Ng, X. Yuan, and W. Zhang. Coupled variational image decomposition and restoration model for blurred ccartoon-plus-texture images with missing pixels. *IEEE Trans. Image Process.*, 22(6):2233–2246, 2013. 5, 6

[23] I. Omer and M. Werman. Color lines: image specific color representation. In *Proc. CVPR*, pages 946–953, 2004. 1

[24] S. Ono, T. Miyata, I. Yamada, and K. Yamaoka. Image recovery by decomposition with component-wise regularization. *IEICE Trans. Fundamentals.*, E95-A(12):2470–2478, 2012. 6

[25] S. Ono, T. Miyata, I. Yamada, and K. Yamaoka. Missing region recovery by promoting blockwise low-rankness. In *Proc. of IEEE ICASSP*, pages 1281–1284, 2012. 6

[26] S. Ono and I. Yamada. Poisson image restoration with likelihood constraint via hybrid steepest descent method. In *Proc. IEEE ICASSP*, 2013. 6

[27] H. Schaeffer and S. Osher. A low patch-rank interpretation of texture. *SIAM J. Imag. Sci.*, 6(1):226–262, 2013. 6

[28] G. Sharma, W. Wu, and E. N. Dalal. The CIEDE2000 color-difference formula: Implementation notes, supplementary test data, and mathematical observations. *Color Res. and App.*, 30(1):21–30, 2005. 3

[29] L. Shen and C. Yeo. Intrinsic images decomposition using a alocal and global sparse representation of reflectance. In *Proc. CVPR*, pages 697–704, 2011. 1

[30] K. Shirai, M. Okuda, and M. Ikehara. Color-line vector field and local color component decomposition for smoothing and denoising of color images. In *Proc. ICPR*, pages 3050–3053, 2012. 1

[31] E. Stekalovskiy, A. Chambolle, and D. Cremers. A convex representation for the vectorial Mumford-Shah functional. In *Proc. CVPR*, pages 1712–1719, 2012. 6

[32] I. Yamada, M. Yukawa, and M. Yamagishi. Minimizing the Moreau envelope of nonsmooth convex functions over the fixed point set of certain quasi-nonexpansive mappings. In H. H. Bauschke, R. S. Burachik, P. L. Combettes, V. Elser, D. R. Luke, and H. Wolkowicz, editors, *Fixed-Point Algorithm for Inverse Problems in Science and Engineering*, pages 345–390. Springer-Verlag, 2011. 3